Lawrence Berkeley National Laboratory
LBL Publications

Title
Internal Structure of the Central Garlock Fault Zone From Ridgecrest Aftershocks Recorded by Dense Linear Seismic Arrays

Permalink
https://escholarship.org/uc/item/8rd738th

Journal
Geophysical Research Letters, 50(2)

ISSN
0094-8276

Authors
Qiu, Hongrui
Chi, Benxin
Ben-Zion, Yehuda

Publication Date
2023-01-28

DOI
10.1029/2022gl101761

Copyright Information

Peer reviewed

AGU
ADVANCING EARTH AND SPACE SCIENCE

Geophysical Research Letters®

Key Points:

- We image the central Garlock fault using data of aftershocks of the 2019 Ridgecrest earthquake recorded by two dense linear arrays
- A *P*-wave velocity contrast across the fault (~5% faster in the north) generates clear fault zone head and reflected waves
- Kirchhoff migration of *P* waves reflected by the fault indicates a near-vertical interface with a sharp impedance contrast

Internal Structure of the Central Garlock Fault Zone From Ridgecrest Aftershocks Recorded by Dense Linear Seismic Arrays

Hongrui Qiu[1,2] ✦, Benxin Chi[3] ✦, and Yehuda Ben-Zion[4,5] ✦

[1]Earth, Atmospheric and Planetary Sciences, Massachusetts Institute of Technology, Cambridge, MA, USA, [2]Now at Earth and Environmental Sciences Area, Lawrence Berkeley National Laboratory, Berkeley, CA, USA, [3]State Key Laboratory of Geodesy and Earth's Dynamics, Innovation Academy for Precision Measurement Science and Technology, Chinese Academy of Sciences, Wuhan, China, [4]Department of Earth Sciences, University of Southern California, Los Angeles, CA, USA, [5]Southern California Earthquake Center, University of Southern California, Los Angeles, CA, USA

Abstract We provide high-resolution seismic imaging of the central Garlock fault using data recorded by two dense seismic arrays that cross the Ridgecrest rupture zone (B4) and the Garlock fault (A5). Analyses of fault zone head waves and *P*-wave delay times at array A5 show that the Garlock fault is a sharp bimaterial interface with *P* waves traveling ~5% faster in the northern crustal block. The across-fault velocity contrast agrees with regional tomography models and generates clear *P*-wave reflections in waveforms recorded by array B4. Kirchhoff migration of the reflected waves indicates a near-vertical fault between 2 and 6 km depth. The *P*-wave delay times imply a ~300-m-wide transition zone near the Garlock fault surface trace beneath array A5, offset to the side with faster velocities. The results provide important constraints for derivations of earthquake properties, simulations of ruptures and ground motion, and future imaging studies associated with the Garlock fault.

Plain Language Summary Along the northern edge of the Mojave Desert, the Garlock fault intersects the San Andreas fault and is the second largest (~300 km long) fault in Southern California. It can host *M* > 7 earthquakes that pose significant seismic hazard to densely populated communities. However, the subsurface structure of the Garlock fault is not well understood due to the sparse seismic network and lack of seismic activity nearby. The 2019 Ridgecrest earthquake sequence in the Eastern California Shear Zone led to a rapid deployment of several dense linear arrays with ~100 m spacing and apertures of a few kilometers, which cross the Ridgecrest rupture zone and also the Garlock fault. The recorded seismic data is used here to illuminate the internal structure of the central Garlock fault. Analyses of *P*-wave delay times and waves refracted along and reflected by the fault interface indicate a near-vertical Garlock fault that separates two distinctive crustal blocks with different wave speeds. The resolved high-resolution fault zone image can have important implications for multiple studies associated with the Garlock fault.

1. Introduction

The left-lateral Garlock fault at the edge of the Mojave block is a significant component of the tectonic region between the Pacific and North American plates in Southern California. Although less active seismically compared to other large faults in the plate boundary (e.g., SAF—San Andreas fault, San Jacinto fault, and ECSZ—Eastern California Shear Zone) during the past several decades (e.g., Hauksson et al., 2012), the Garlock fault is large enough to produce major (e.g., *Mw* > 7.5) earthquakes. Previous paleo-seismic studies (e.g., Dawson et al., 2003; Madugo et al., 2012) found that surface-rupturing earthquakes along the central Garlock fault are highly clustered in time, which may reflect interactions between the Garlock fault and the big bend section of the SAF or faults in the ECSZ.

Detailed information about the subsurface structure of the Garlock fault (e.g., across-fault velocity contrast, dip, and damage zone properties) can improve the accuracy of locations, focal mechanisms, and other parameters derived for earthquakes on the fault (e.g., McGuire & Ben-Zion, 2005; McNally & McEvilly, 1977; Oppenheimer et al., 1988), contribute to the understanding of spatio-temporal earthquake patterns (Abdelmeguid & Elbanna, 2022; Brietzke & Ben-Zion, 2006; Thakur & Huang, 2021; Thakur et al., 2020), and provide constraints for modeling future ruptures and expected ground motion (e.g., Blisniuk et al., 2021; Brietzke et al., 2009; Fuis
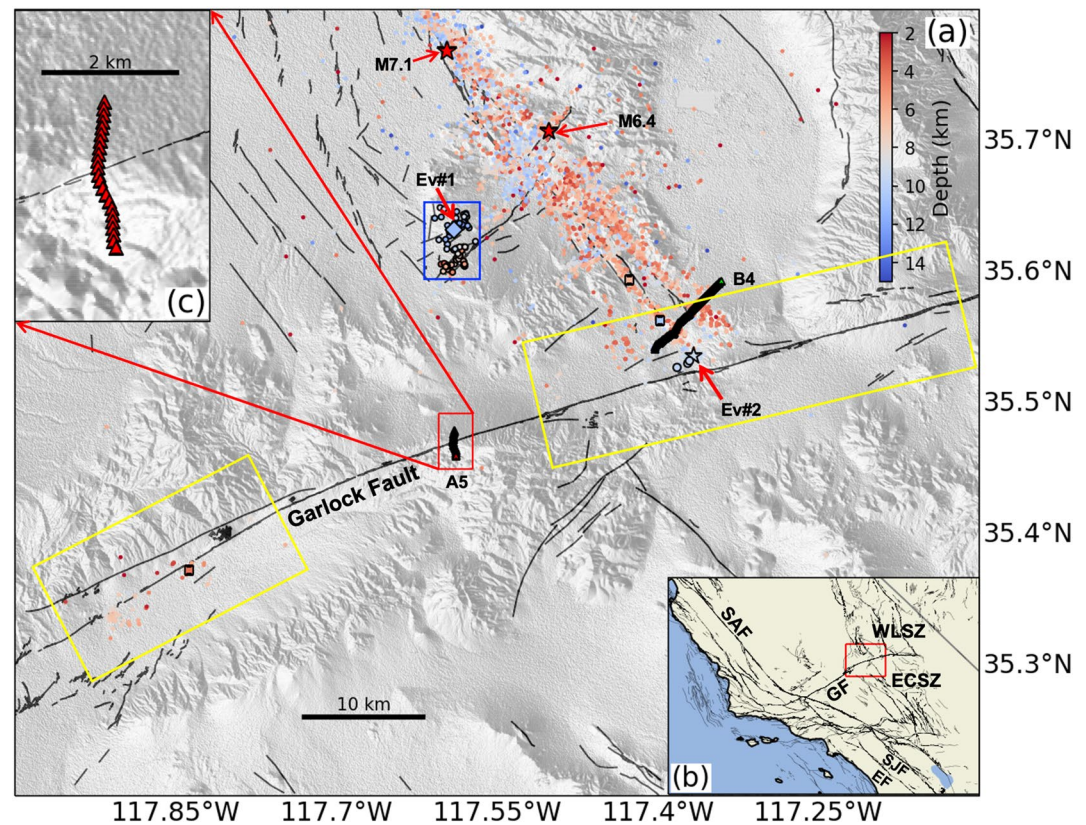
Figure 1. (a) Location map for the central Garlock fault, the 2019 Ridgecrest earthquake sequence (colored dots), and two fault zone linear arrays (B4 and A5; triangles) analyzed in this study. Red stars mark epicenters of the 2019 Mw6.4 and Mw7.1 Ridgecrest earthquakes. Events outlined by blue and yellow boxes are used in the analyses of *P*-wave delay times and fault zone head waves, respectively. The catalog of Hauksson et al. (2012, extended to 2019) is used for event locations. (b) Map of southern and central California with the red box indicating the study area shown in panel (a). (c) Configuration of array A5 that crosses the Garlock fault. SAF, San Andreas fault; GF, Garlock fault; SJF, San Jacinto fault; EF, Elsinore fault; WLSZ, Walker Lane Shear Zone; ECSZ, Eastern California Shear Zone.

et al., 2012; Share & Ben-Zion, 2018). Moreover, recent studies have shown that local variations of seismic properties of fault zone structures can affect the wavefield far from the fault (e.g., Schliwa & Gabriel, 2022; Yeh & Olsen, 2022).

Recordings of dense fault zone arrays deployed across or near fault surface traces allow derivations of detailed structural images including information on velocity contrast interfaces and fault damage zones (e.g., Qiu et al., 2021; Zhao et al., 2010). However, the lack of dense recordings and insufficient seismic events near the Garlock fault have made it challenging to image the internal structure of the Garlock fault before 2019. The Ridgecrest earthquake sequence that occurred in 2019 and several rapid deployments of dense arrays around the Garlock fault (Catchings et al., 2020) provide the necessary data for high-resolution imaging of key structural properties of the central Garlock fault (Figure 1a).

In the present paper, we use waveforms of aftershocks recorded by dense arrays across the Garlock fault and the rupture zone of the 2019 Mw7.1 Ridgecrest earthquake to image the velocity contrast, surrounding structure, and dip of the central Garlock fault. We perform several analyses using *P*-wave delay times (Section 3.1), fault zone head waves (FZHWs; Section 3.2), and *P* waves reflected by the Garlock fault (Section 3.3). The results indicate that the analyzed section of the Garlock fault (between arrays A5 and B4 in Figure 1) is a sharp bimaterial inter- face (faster seismic velocity in the north), with a near-vertical dip that extends at least to 8 km. A ~300-m-wide low-velocity zone is also imaged near the surface trace of the central Garlock fault; however, the lack of fault zone trapped waves in recordings at stations within the low-velocity zone suggests that it is internally heterogeneous or may be associated with a shallow fault-related sedimentary basin rather than a fault damage zone. The resolved structural features (across-fault velocity contrast, fault dip, and asymmetric low-velocity zone) provide important

benchmarks for future imaging of the Garlock fault, along with key information for improved derivations of earthquake source parameters and simulations of ruptures and ground motion associated with the fault.

2. Data

Several linear arrays, with about 100 m station spacing and apertures of 2–8 km, were deployed in the rupture zone of the 2019 Ridgecrest earthquake and across surface traces of the Garlock fault (Catchings et al., 2020). All the arrays consisted of three-component sensors and recorded continuously at 500 Hz for about 1 month after the 2019 Mw7.1 mainshock. Here, we use data from two linear arrays A5 and B4 (Figure 1) to image the internal structure of the Garlock fault. As pre-processing steps, we first demean and detrend the waveforms of teleseismic and local earthquakes recorded by the two arrays. A bandpass filter between 0.5 and 20 Hz is then applied to increase the signal to noise ratio (SNR). Data recorded by array A5, which crosses the surface trace of the Garlock fault, are used in analyses of *P*-wave delay times (Section 3.1) and FZHWs (Section 3.2). Fault zone reflected waves (FZRWs), involving *P* waves reflected by the Garlock fault and recorded at array B4, are utilized to infer the subsurface geometry of the Garlock fault (Section 3.3).

3. Results

3.1. Delay Time Analysis of *P*-Wave

The delay time pattern of *P* or *S* waves with a near-vertical incident angle provides a first-order estimation of the velocity structure beneath the recording array averaged over the top few kilometers (e.g., Ozakin et al., 2012; Qiu et al., 2021). We only focus on *P* waves, although delay times of *S* waves have been analyzed before (e.g., Yang et al., 2020), as the accuracy of *S* wave picking is considerably lower due to *P*-wave coda and radial anisotropy. In this section, we measure *P*-wave delay times using teleseismic and local earthquakes recorded by array A5 to infer the velocity variation (e.g., across-fault velocity contrast) of the Garlock fault zone along the fault-normal direction beneath the array.

For teleseismic earthquakes, we select events with *Mw* > 6.0, depth >50 km, and epicentral distances between 30° and 90°. Three teleseismic events (stars in Figure S1 in Supporting Information S1) with sufficient SNR are found during the recording period of array A5 and included in the analysis. Following the procedure of Qiu et al. (2021) used for the Ridgecrest rupture zone, we first truncate and align the teleseismic *P* waves according to theoretical arrival times calculated using the IASP91 model (Kennett & Engdahl, 1991). Then, we cross-correlate the early *P* waveforms between every pair of stations, correct for topography, and estimate the delay times of teleseismic *P* waves due to fault zone structures beneath array A5.

Next, we take advantage of the vigorous aftershocks in the 2019 Ridgecrest earthquake sequence. To ensure the incoming *P* waves enter the fault zone beneath array A5 with a near-vertical incidence angle, ~100 aftershocks (within the blue box in Figure 1) north of the recording array are selected for this analysis. Adopting the procedure of Qiu et al. (2021), we measure the local *P*-wave delay times (e.g., Figure S2 in Supporting Information S1) with the following steps: (a) pick the *P*-wave arrival time, t_{ij} for station i and event j, via the STA/LTA algorithm (Allen, 1978); (b) convert the arrival time to the average slowness s_{ij} by dividing the corresponding hypocentral distance H_{ij}, that is, $s_{ij} = t_{ij}/H_{ij}$, and compute the array-mean slowness $\bar{s}_j = \sum_{i=1}^{M} s_{ij}/M$ with M being the total number of stations; and (c) measure the delay time pattern due to local velocity structures beneath array A5 as $\delta t_{ij} = (s_{ij} - \bar{s}_j) \cdot H_{ij}$.

Figure 2a shows the *P*-wave delay time patterns averaged over all analyzed teleseismic (in gray) and local (in black) events. Both sets of results show consistently a larger *P*-wave delay time at stations south of the fault surface trace and suggest that the Garlock fault separates two crustal blocks with different *P*-wave velocities (lower in the southern block). Between the two distinctive crustal blocks, there is a ~300-m-wide transition zone north (faster side) of the fault surface trace (rather than at the center). Consistent with observations for other fault and rupture zones (e.g., Lewis et al., 2005; Qin et al., 2018; Qiu et al., 2021), this is likely indicative of asymmetric rock damage generated by earthquake ruptures. Since the frequency is much higher for *P* waves from local earthquakes (~10 Hz; Figure S2 in Supporting Information S1) than teleseismic events (0.5–2 Hz; Figure S1 in Supporting Information S1), the local *P*-wave delay times (black dots in Figure 2a) provide an image of the internal fault zone structure with much higher spatial resolution. Thus, we further identify a ~300-m-wide
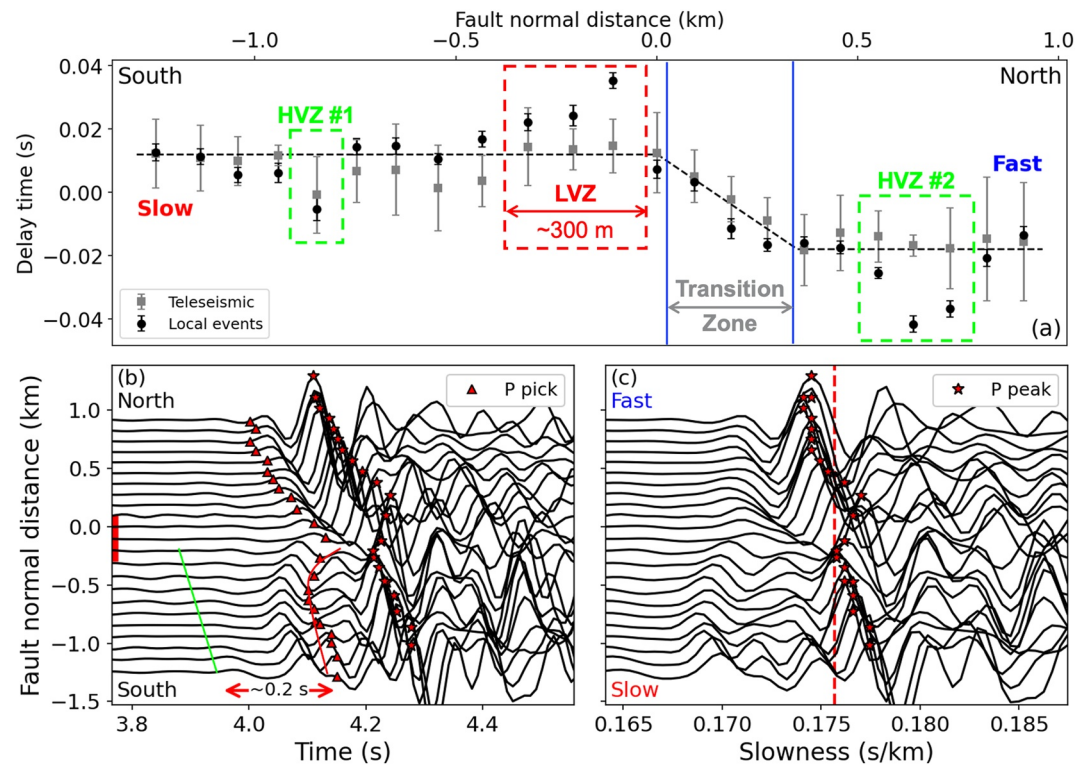
Figure 2. (a) Delay time patterns of *P*-wave averaged over all analyzed teleseismic (in gray) and local (in black) earthquakes. Error bars denote ± two standard deviations around the corresponding mean values. The gray dashed lines outline the across-fault velocity contrast with a ~300-m-wide transition zone. The dashed boxes highlight a low-velocity zone (in red) and two high-velocity zones (in green). (b) *P* waveforms of an example event (the star in the yellow box in Figure 1a) with reliable fault zone head wave (FZHW) detections. Red stars denote the arrival time of the direct *P*-wave peaks (t_{peak}). The red triangles represent the shifted peak times, $t_{peak} - 3T/4$, with T being the dominant period of the early *P* waveforms and are used to approximate the onset of direct *P* waves. The green line delineates the FZHW picks and Δt_{F2D} is given by the time difference between the green and red curves. The red bar depicts the span of the low-velocity zone found in panel (a). Panel (c) same as panel (b), but in the slowness domain.

low-velocity zone (red dashed box) and two narrow zones with faster velocity anomalies (green dashed boxes) in Figure 2a. Detailed information about how the across-fault velocity contrast (black dashed line) and narrow anomalous velocity zones (dashed boxes) are identified can be found in Qiu et al. (2021).

3.2. Fault Zone Head Waves

A sharp across-fault velocity contrast produces FZHWs, which are refracted phases propagating exclusively along the fault interface. Compared to the direct *P* waves, FZHWs have lower amplitude and dominant frequency and are the first-arriving phase only when receivers are on the slower side of the fault within a critical fault-normal distance (Ben-Zion, 1989, 1990). FZHWs also have a different horizontal particle motion than the direct *P* waves (e.g., Bulut et al., 2012). When FZHWs are the first-arriving phase, the differential time between them and direct *P* arrivals, Δt_{F2D}, depends on the source and receiver locations (e.g., Ben-Zion & Malin, 1991). Let d_s and d_r be the fault-normal distance of the earthquake and receiver, Δt_{F2D} decreases if either d_s or d_r increases (Share & Ben-Zion, 2016). The detection of FZHW utilizes some or all these features and often focuses only on recordings of close-to-fault events and stations to increase Δt_{F2D} (and thus the detectability). If both d_s and d_r are much smaller than the hypocentral distance R_{sr}, the differential time is approximately given by

$$\Delta t_{F2D} \approx R_{sr} \cdot \Delta\alpha/\alpha^2, \tag{1}$$

where $\Delta\alpha$ and α are the differential and average velocities, respectively (Ben-Zion & Malin, 1991). Equation 1 can be further simplified to be

$$\Delta t_{\text{F2D}} \approx \eta \cdot t_D, \tag{2}$$

where η and t_D denote the across-fault velocity contrast ($\approx \Delta\alpha/\alpha$) and the direct wave arrival time ($\approx R_{sl}/\alpha$), respectively.

Since *S*-type FZHWs (i.e., *S* waves refracted along the fault interface) are much more difficult to detect and verify due to *P*-wave coda and radial anisotropy, we only focus on the *P*-type FZHWs. We first apply an automated phase picker (Ross & Ben-Zion, 2014) to detect candidate FZHWs in *P* waveforms recorded by array A5 for events sufficiently close to the Garlock fault (yellow rectangles in Figure 1a). Then, we further examine each *P* waveform with FZHW detection and confirm that the first-arriving emergent phase does have a particle motion polarization different from the later impulsive arrival (e.g., Allam et al., 2014). Finally, we visually inspect *P* waveforms recorded at the entire array for each candidate event that passes these selection criteria and verify that only stations on one side of the Garlock fault show FZHWs.

Figure 2b shows *P* waveforms for an FZHW-generating candidate event less than 1 km away from the Garlock fault that passes all selection criteria. Clear FZHWs are observed ∼0.2 s before direct *P* waves and only at stations south of the surface trace, which is consistent with the results of delay time analysis that *P* waves travel slower in the southern crustal block (Figure 2a). Similar FZHW detections are found in recordings of three nearby events (Figure S3 in Supporting Information S1). In contrast to FZHWs generated at the edge of fault damage zones (i.e., Δt_{F2D} decreases rapidly with fault-normal distance; Qiu et al., 2017), less than a 10% decrease in Δt_{F2D} is observed within the southern part of array A5 (Figure 2b). We also detect FZHWs generated by events ∼3–4 km away from the Garlock fault but with much smaller Δt_{F2D} (e.g., <0.1 s in Figure S4b in Supporting Information S1). These observations further confirm the reliability of the FZHW detections and the existence of a sharp velocity contrast across the imaged section of the Garlock fault with an average η of ∼5% in the top ∼8 km (≈0.2/4; Figure 2b, Equation 2). We do not find any FZHWs in *P* waveforms from events southwest of array A5, suggesting the sharp velocity contrast across the Garlock fault between arrays A5 and B4 likely does not extend further west beyond where the surface trace bifurcates (Figure 1a).

3.3. Kirchhoff Migration of Fault Zone Reflected Waves

The sharp velocity contrast across the Garlock fault not only generates FZHWs but also acts as a reflection interface. While imaging the rupture zone of the 2019 Mw7.1 Ridgecrest earthquake, Qiu et al. (2021) found coherent secondary arrivals between *P* and *S* arrivals in recordings of array B4 (e.g., Figures 3b and 3c). They attributed these secondary phases to *P* waves reflected by the Garlock fault, as the observed arrival times match well with the prediction (blue curve in Figure 3b). Here, we further validate that these secondary arrivals are indeed FZRWs by comparing the back-azimuths calculated via raytracing (e.g., blue arrow in Figure 3a) and measured from the particle motion polarization analysis of the FZRWs recorded at station B444 in Figure S5 in Supporting Information S1. In total, we identify seven events (circles and the star in Figure 3a) with high-quality FZRWs recorded by array B4 with arrival times matching well with the prediction from ray tracing (Figure 3b, Figure S6 in Supporting Information S1).

The arrival times of reflected waves are sensitive to the location of the reflector and are often utilized to image subsurface interfaces with sharp impedance contrast. Here, we adopt the well-developed Kirchhoff migration method (Schneider, 1978; Sheehan et al., 2000) to image the subsurface geometry of the Garlock fault using the FZRWs shown in Figure 3b and Figure S6 in Supporting Information S1. For each event, we (a) first apply a tapering window around high-quality FZRWs and compute the backward wavefield by back propagating the tapered FZRWs to each image point; (b) then calculate the forward wavefield by placing a source wavelet at the event origin time and hypocenter location; (c) correlate snapshots of these two wavefields at each time step and integrate in time the wavefield correlations to get the initial image $I(x,y,z)$; and (d) compute the final image as the square of the envelope function of the initial image $I(x,y,z)$ normalized by its maximum value. We note that both the forward and backward wavefields are calculated by solving the eikonal equation using the regional velocity model CVM-H15.1 (Shaw et al., 2015). Figure S7 in Supporting Information S1 shows the final migration results in the map view at depths between 2 and 7 km.

Figure 4 shows the final migration image averaged over all seven events in the map view at 4 km depth (Figure 4c) and along a certain meridian (Figure 4d). Due to smearing caused by the limited spatial distribution of source and receiver, nonzero values are also seen in the image for areas that are not covered by the propagation paths
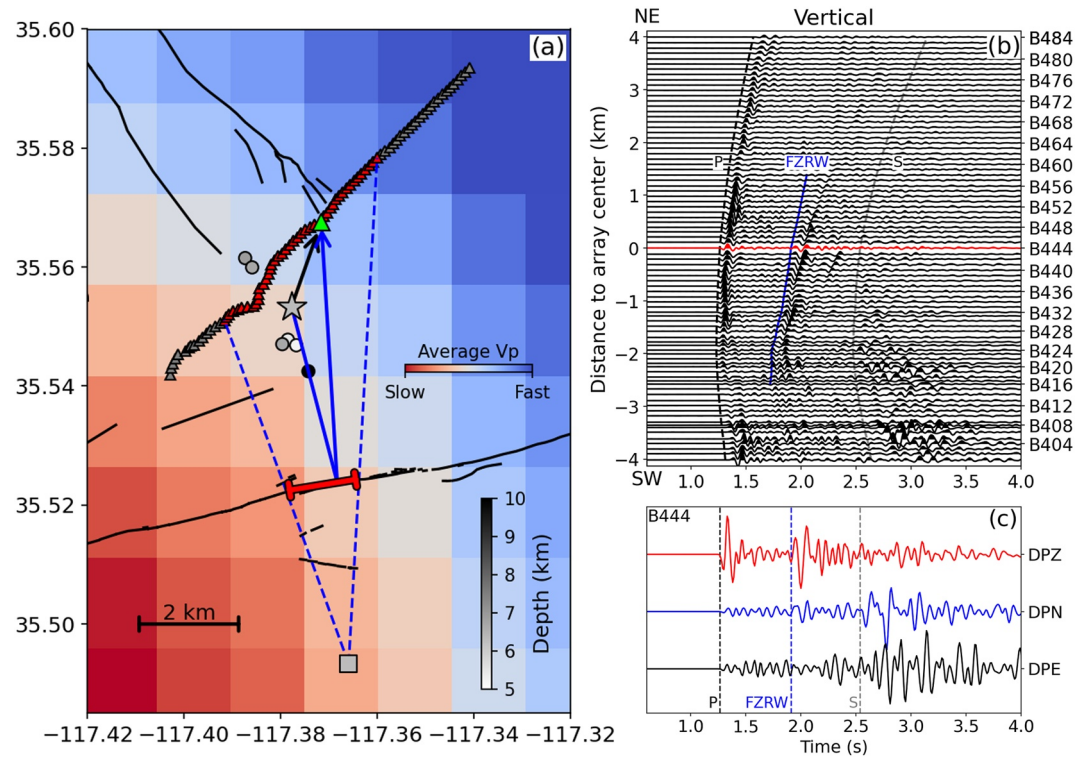
Figure 3. *P* waves reflected by the Garlock fault recorded at array B4. (a) Location map of array B4 (triangles), fault surface traces (black lines), and events (star and circles) that generate fault zone reflected waves (FZRWs). The color of each event and in the background indicate the focal depth and *P*-wave velocity (*Vp*) of the CVM-H15.1 averaged over 2–15 km depth, respectively. The square denotes the effective source location for the FZRWs of the event shown as the star. The black and blue arrows delineate propagation paths calculated via ray tracing for the direct and reflected *P* waves recorded at station B444 (in green) in map view. (b) Vertical component waveforms of the event shown as the star in panel (a). Stations with clear FZRWs between *P* and *S* arrivals (dashed curves) are shown as red triangles in panel (a). The blue curve denotes the synthetic arrival times of the FZRWs if a constant *Vp* (≈5.6 km/s) and a vertical bimaterial Garlock fault are assumed. (c) Recordings of all three components at station B444. *P* and FZRW denote synthetic arrival times of the direct *P*-wave and the reflection from the Garlock fault.

of FZRWs. Following large values (e.g., >0.5) of the image near the surface trace, we delineate the location of the Garlock fault as the red bar within the depth range (3–6 km) that the FZRWs are sensitive to. The migration analysis suggests that the Garlock fault in the vicinity of array B4 is a near-vertical interface right beneath the mapped surface trace with a sharp impedance contrast extending to at least ∼6 km depth.

4. Discussion and Conclusions

We image several key structural components of the central Garlock fault zone, with high spatial resolution of ∼100 m and less, including low- and high-velocity zones and a large-scale bimaterial interface. Consistent with the CVM-15.1 regional velocity model (colors in Figure 4a), the imaged section of the Garlock fault separates two distinctive crustal blocks with a lower *P*-wave velocity (*Vp*) in the south. However, our results indicate unambiguously that the velocity contrast involves a sharp bimaterial interface rather than a gradual contrast zone. The detection and analysis of FZHWs demonstrate that the bimaterial interface is continuous along the section of the Garlock fault between arrays A5 and B4. The bimaterial interface produces clear *P*-wave delay times at array A5 (Figure 2a), while analysis of FZRWs indicate a vertical interface with a strong impedance contrast south of array B4 (Figures 4c and 4d). The migration of FZRWs from the examined earthquakes implies that the Garlock fault is near-vertical to a depth of at least 6 km (Figure 4c).

The results indicate an average 5% contrast of *Vp* across the Garlock fault over the propagation distance and depth section between the events and arrays (Figure 2b). The depths of events that generate FZHWs imply that the bimaterial interface extends to at least 8 km (Figure 1a). The sense of velocity contrast and left-lateral motion across the central Garlock fault suggest a preferred propagation direction of subshear earthquake ruptures to the
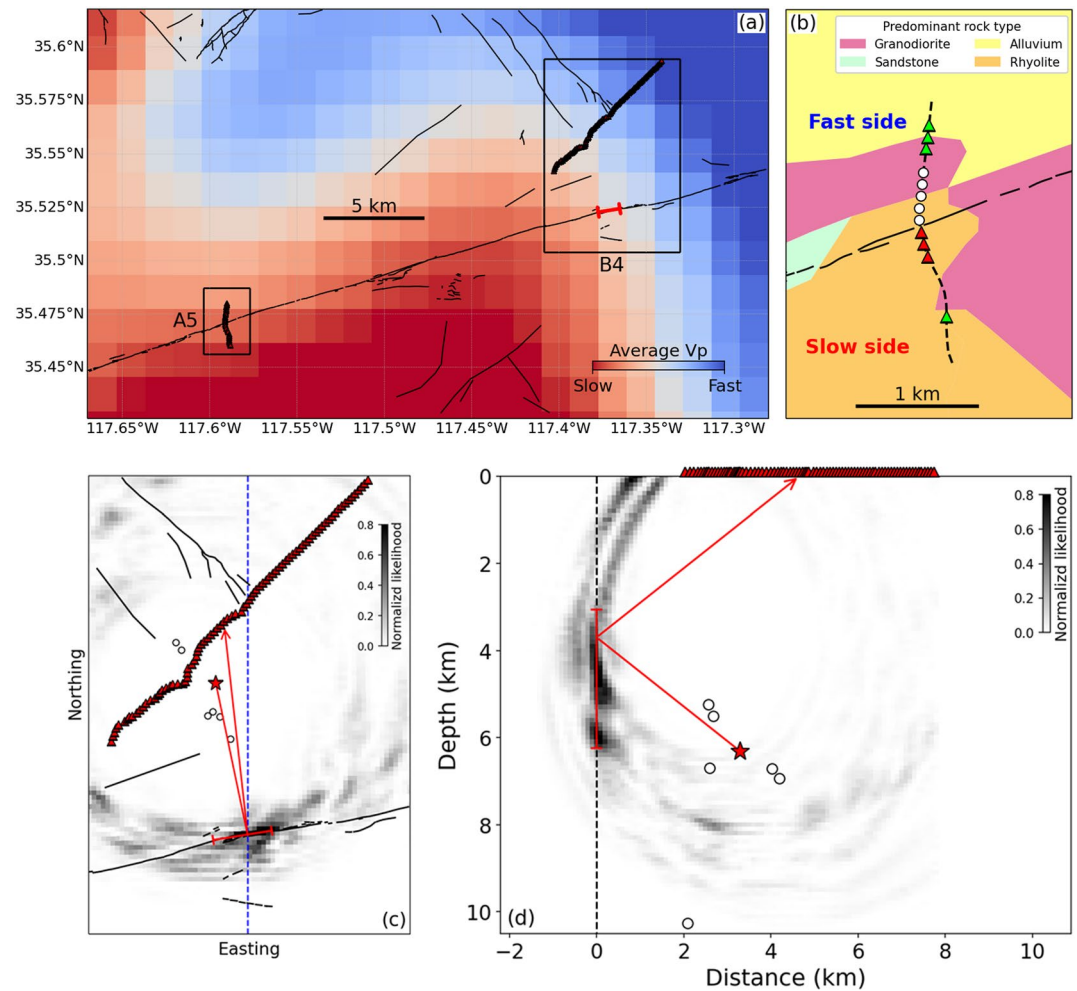
Figure 4. Results of fault zone imaging for the Garlock fault. (a) Location map of arrays B4 and A5 (triangles) and fault surface traces (black lines). The background color illustrates the map of average *P*-wave velocities (Figure 3a). (b) Zoom in map around array A5 with the dashed curve representing the array configuration. The velocity contrast across the Garlock fault is labeled, with white circles indicating the span of the transition zone. The red and green triangles highlight stations within the narrow low- and high-velocity zones, respectively. Results for the Kirchhoff migration of fault zone reflected waves observed in Figure 3b and Figure S6 in Supporting Information S1 are shown in panels (c and d) at 4 km depth and along a certain meridian (blue dashed line), respectively. The red bar denotes the bimaterial Garlock fault interface inferred from the migration image.

east-north-east, and an opposite preferred direction for supershear ruptures (Aichele et al., 2022; Andrews & Ben-Zion, 1997; Shi & Ben-Zion, 2006; Weertman, 1980, 2002). The velocity contrast interface likely does not extend continuously beyond array A5 in the southwest, as FZHW detections were not found for events southwest of array A5.

In addition to the across-fault velocity contrast, the *P*-wave delay time analysis reveals a ∼300-m-wide transition zone, a ∼300-m-wide low-velocity zone, and two narrow high-velocity zones in structures beneath array A5 (Figures 2a and 4b). The location of the transition zone (white circles in Figure 4b) matches the theoretical expectation of asymmetric rock damage existing primarily on the side of the fault with higher seismic velocities at depth (e.g., Ben-Zion & Shi, 2005). Despite the mismatch in exact locations, a similar pattern of rock types (rhyolite and granodiorite) correlates with the spatial distribution of low- and high-velocity zones (triangles). These narrow zones are likely representative of shallow materials and are consistent with no fault zone trapped wave detections in the data recorded by array A5. The lack of trapped waves likely indicates the fault zone beneath the array is too heterogeneous to generate trapped waves (e.g., Lewis & Ben-Zion, 2010).

The polarity and amplitude of direct and reflected waves are sensitive to the impedance contrast across the reflection interface and may be used to constrain further the across-fault velocity contrast. However, the relative polarity and amplitude ratio between the two phases depends on various additional factors, such as the focal mechanism and attenuation, and are left for future studies. A future study may also use the observed direct and FZHWs to derive information on the depth variation of the velocity contrast across the Garlock fault (e.g., Ben-Zion et al., 1992). We note that reflected *S* waves are also observed in recordings of array B4, but we exclude them from this study as the SNR is low due to *P*-wave coda and *P*-to-*S* conversions.

The key results of this study and their relevance to various topics are:

1. The inferred velocity contrast can produce statistically preferred rupture propagation directions of earthquakes (to the east-north-east for standard subshear ruptures and to the west-south-west for supershear ruptures) on the imaged section of the Garlock fault. This may influence significantly the spatial distribution of the radiated seismic waves and sequences of earthquakes on the fault (e.g., Abdelmeguid & Elbanna, 2022; Ampuero & Ben-Zion, 2008; Brietzke et al., 2009; Shlomai & Fineberg, 2016).
2. The bimaterial interface is continuous along the imaged section of the fault but likely terminates at some point southwest of array A5. This change in the fault interface properties can arrest ruptures and affect the interactions between the Garlock fault and the SAF (e.g., Brietzke & Ben-Zion, 2006; Share & Ben-Zion, 2016, 2018).
3. The imaging results provide key information for derivations of source properties of earthquakes on the central Garlock fault (e.g., McGuire & Ben-Zion, 2005; McNally & McEvilly, 1977; Oppenheimer et al., 1988), and have implications for the seismic wavefield generated at significant distances from the fault (e.g., Fuis et al., 2012; Schliwa & Gabriel, 2022; Yeh & Olsen, 2022).

While the obtained imaging results cover a limited section of the Garlock fault, the high-resolution information (near-vertical dip, sharp velocity contrast, and imaged local low- and high-velocity zones) provide strong benchmarks for interpretation of regional velocity models in this area (e.g., Tong et al., 2021), and future imaging of the Garlock fault zone using distributed acoustic sensing (Atterholt et al., 2022) and other techniques.

Data Availability Statement

Data described in this paper are available from the IRIS Data Management Center (https://ds.iris.edu/mda/3J/). Detail of array data acquisition is available from Catchings et al. (2020). The geologic data shown in Figure 4b were obtained from the USGS website (https://mrdata.usgs.gov/geology/state/state.php?state=CA).

References

Abdelmeguid, M., & Elbanna, A. (2022). Sequences of seismic and aseismic slip on bimaterial faults show dominant rupture asymmetry and potential for elevated seismic hazard. *Earth and Planetary Science Letters*, *593*, 117648. https://doi.org/10.1016/j.epsl.2022.117648

Aichele, J., Latour, S., Catheline, S., & Roux, P. (2022). Dynamic full-field imaging of rupture radiation: Material contrast governs source mechanism. *Geophysical Research Letters*, *49*, e2022GL100473. https://doi.org/10.1029/2022GL100473

Allam, A. A., Ben-Zion, Y., & Peng, Z. (2014). Seismic imaging of a bimaterial interface along the Hayward fault, CA, with fault zone head waves and direct P arrivals. *Pure and Applied Geophysics*, *171*(11), 2993–3011. https://doi.org/10.1007/s00024-014-0784-0

Allen, R. (1978). Automatic earthquake recognition and timing from single traces. *Bulletin of the Seismological Society of America*, *68*(5), 1521–1532. https://doi.org/10.1785/bssa0680051521

Ampuero, J. P., & Ben-Zion, Y. (2008). Cracks, pulses and macroscopic asymmetry of dynamic rupture on a bimaterial interface with velocity-weakening friction. *Geophysical Journal International*, *173*(2), 674–692. https://doi.org/10.1111/j.1365-246X.2008.03736.x

Andrews, D. J., & Ben-Zion, Y. (1997). Wrinkle-like slip pulse on a fault between different materials. *Journal of Geophysical Research*, *102*(B1), 553–571. https://doi.org/10.1029/96jb02856

Atterholt, J. W., Zhan, Z., & Yang, Y. (2022). Imaging the Garlock Fault Zone using distributed acoustic sensing. *Poster Presentation at 2022 SCEC Annual Meeting*. Retrieved from https://www.scec.org/publication/12369

Ben-Zion, Y. (1989). The response of two joined quarter spaces to SH line sources located at the material discontinuity interface. *Geophysical Journal International*, *98*(2), 213–222. https://doi.org/10.1111/j.1365-246x.1989.tb03346.x

Ben-Zion, Y. (1990). The response of two half spaces to point dislocations at the material interface. *Geophysical Journal International*, *101*(3), 507–528. https://doi.org/10.1111/j.1365-246x.1990.tb05567.x

Ben-Zion, Y., Katz, S., & Leary, P. (1992). Joint inversion of fault zone head waves and direct P arrivals for crustal structure near major faults. *Journal of Geophysical Research*, *97*(B2), 1943–1951. https://doi.org/10.1029/91JB02748

Ben-Zion, Y., & Malin, P. (1991). San Andreas fault zone head waves near Parkfield, California. *Science*, *251*(5001), 1592–1594. https://doi.org/10.1126/science.251.5001.1592

Ben-Zion, Y., & Shi, Z. (2005). Dynamic rupture on a material interface with spontaneous generation of plastic strain in the bulk. *Earth and Planetary Science Letters*, *236*(1–2), 486–496. https://doi.org/10.1016/j.epsl.2005.03.025

Blisniuk, K., Scharer, K., Sharp, W. D., Burgmann, R., Amos, C., & Rymer, M. (2021). A revised position for the primary strand of the Pleistocene-Holocene San Andreas fault in southern California. *Science Advances*, *7*(13), eaaz5691. https://doi.org/10.1126/sciadv.aaz5691

Brietzke, G. B., & Ben-Zion, Y. (2006). Examining tendencies of in-plane rupture to migrate to material interfaces. *Geophysical Journal International*, *167*(2), 807–819. https://doi.org/10.1111/j.1365-246X.2006.03137.x

Brietzke, G. B., Cochard, A., & Igel, H. (2009). Importance of bimaterial interfaces for earthquake dynamics and strong ground motion. *Geophysical Journal International*, *178*(2), 921–938. https://doi.org/10.1111/j.1365-246X.2009.04209.x

Bulut, F., Ben-Zion, Y., & Bohnhoff, M. (2012). Evidence for a bimaterial interface along the Mudurnu segment of the North Anatolian fault zone from polarization analysis of P waves. *Earth and Planetary Science Letters*, *327–328*, 17–22. https://doi.org/10.1016/j.epsl.2012.02.001

Catchings, R. D., Goldman, M. R., Steidl, J. H., Chan, J. H., Allam, A. A., Criley, C. J., et al. (2020). Nodal seismograph recordings of the 2019 Ridgecrest earthquake sequence. *Seismological Research Letters*, *91*(6), 3622–3633. https://doi.org/10.1785/0220200203

Dawson, T. E., McGill, S. F., & Rockwell, T. K. (2003). Irregular recurrence of paleoearthquakes along the central Garlock fault near El Paso Peaks, California. *Journal of Geophysical Research*, *108*(B7), 2356. https://doi.org/10.1029/2001JB001744

Fuis, G. S., Scheirer, D. S., Langenheim, V. E., & Kohler, M. D. (2012). A new perspective on the geometry of the San Andreas fault in southern California and its relationship to lithospheric structure. *Bulletin of the Seismological Society of America*, *102*(1), 236–251. https://doi.org/10.1785/0120110041

Hauksson, E., Yang, W., & Shearer, P. M. (2012). Waveform relocated earthquake catalog for Southern California (1981 to June 2011). *Bulletin of the Seismological Society of America*, *102*(5), 2239–2244. https://doi.org/10.1785/0120120010

Kennett, B. L. N., & Engdahl, E. R. (1991). Traveltimes for global earthquake location and phase identification. *Geophysical Journal International*, *105*(2), 429–465. https://doi.org/10.1111/j.1365-246X.1991.tb06724.x

Lewis, M. A., & Ben-Zion, Y. (2010). Diversity of fault zone damage and trapping structures in the Parkfield section of the San Andreas fault from comprehensive analysis of near fault seismograms. *Geophysical Journal International*, *183*(3), 1579–1595. https://doi.org/10.1111/j.1365-246X.2010.04816.x

Lewis, M. A., Peng, Z., Ben-Zion, Y., & Vernon, F. L. (2005). Shallow seismic trapping structure in the San Jacinto fault zone near Anza, California. *Geophysical Journal International*, *162*(3), 867–881. https://doi.org/10.1111/j.1365-246X.2005.02684.x

Madugo, C. M., Dolan, J. F., & Hartleb, R. D. (2012). New paleoearthquake ages from the western Garlock fault: Implications for regional earthquake occurrence in southern California. *Bulletin of the Seismological Society of America*, *102*(6), 2282–2299. https://doi.org/10.1785/0120110310

McGuire, J., & Ben-Zion, Y. (2005). High-resolution imaging of the Bear Valley section of the San Andreas fault at seismogenic depths with fault-zone head waves and relocated seismicity. *Geophysical Journal International*, *163*(1), 152–164. https://doi.org/10.1111/j.1365-246X.2005.02703.x

McNally, K. C., & McEvilly, T. (1977). Velocity contrast across the San Andreas fault in central California: Small-scale variations from P-wave nodal plane distortion. *Bulletin of the Seismological Society of America*, *67*(6), 1565–1576. https://doi.org/10.1785/BSSA0670061565

Oppenheimer, D. H., Reasenberg, P. A., & Simpson, R. W. (1988). Fault plane solutions for the 1984 Morgan Hill, California, earthquake sequence: Evidence for the state of stress on the Calaveras fault. *Journal of Geophysical Research*, *93*(B8), 9007–9026. https://doi.org/10.1029/JB093iB08p09007

Ozakin, Y., Ben-Zion, Y., Aktar, M., Karabulut, H., & Peng, Z. (2012). Velocity contrast across the 1944 rupture zone of the North Anatolian fault east of Ismetpasa from analysis of teleseismic arrivals. *Geophysical Research Letters*, *39*(8), L08307. https://doi.org/10.1029/2012GL051426

Qin, L., Ben-Zion, Y., Qiu, H., Share, P. E., Ross, Z. E., & Vernon, F. L. (2018). Internal structure of the San Jacinto fault zone in the trifurcation area southeast of Anza, California, from data of dense seismic arrays. *Geophysical Journal International*, *213*(1), 98–114. https://doi.org/10.1093/gji/ggx540

Qiu, H., Ben-Zion, Y., Catchings, R., Goldman, M. R., Allam, A. A., & Steidl, J. (2021). Seismic imaging of the Mw7.1 Ridgecrest earthquake rupture zone from data recorded by dense linear arrays. *Journal of Geophysical Research: Solid Earth*, *126*(7), e2021JB022043. https://doi.org/10.1029/2021JB022043

Qiu, H., Ben-Zion, Y., Ross, Z. E., Share, P. E., & Vernon, F. L. (2017). Internal structure of the San Jacinto fault zone at Jackass Flat from data recorded by a dense linear array. *Geophysical Journal International*, *209*(3), 1369–1388. https://doi.org/10.1093/gji/ggx096

Ross, Z., & Ben-Zion, Y. (2014). Automatic picking of direct P, S seismic phases and fault zone head waves. *Geophysical Journal International*, *199*(1), 368–381. https://doi.org/10.1093/gji/ggu2672014

Schliwa, N., & Gabriel, A. (2022). Fault damage zone effects on near-field ground motion parameters and plastic strain in a multi-scale dynamic rupture model of the 2019 Ridgecrest sequence. *Poster Presentation at 2022 SCEC Annual Meeting*. Retrieved from https://www.scec.org/meetings/2022/am/poster/238

Schneider, W. A. (1978). Integral formulation for migration in 2 and 3 dimensions. *Geophysics*, *43*(1), 49–76. https://doi.org/10.1190/1.1440828

Share, P.-E., & Ben-Zion, Y. (2016). Bimaterial interfaces in the South San Andreas fault with opposite velocity contrasts NW and SE from San Gorgonio Pass. *Geophysical Research Letters*, *43*(20), 10680–10687. https://doi.org/10.1002/2016GL070774

Share, P.-E., & Ben-Zion, Y. (2018). A bimaterial interface along the northern San Jacinto fault through Cajon Pass. *Geophysical Research Letters*, *45*(21), 11–622. https://doi.org/10.1029/2018GL079834

Shaw, J. H., Plesch, A., Tape, C., Suess, M. P., Jordan, T. H., Ely, G., et al. (2015). Unified structural representation of the Southern California crust and upper mantle. *Earth and Planetary Science Letters*, *415*, 1–15. https://doi.org/10.1016/j.epsl.2015.01.016

Sheehan, A. F., Shearer, P. M., Gilbert, H. J., & Dueker, K. G. (2000). Seismic migration processing of P-SV converted phases for mantle discontinuity structure beneath the Snake River Plain, western United States. *Journal of Geophysical Research*, *105*(B8), 19055–19065. https://doi.org/10.1029/2000JB900112

Shi, Z., & Ben-Zion, Y. (2006). Dynamic rupture on a bimaterial interface governed by slip-weakening friction. *Geophysical Journal International*, *165*(2), 469–484. https://doi.org/10.1111/j.1365-246X.2006.02853.x

Shlomai, H., & Fineberg, J. (2016). The structure of slip-pulses and supershear ruptures driving slip in bimaterial friction. *Nature Communications*, *7*(1), 11787. https://doi.org/10.1038/ncomms11787

Thakur, P., & Huang, Y. (2021). Influence of fault zone maturity on fully dynamic earthquake cycles. *Geophysical Research Letters*, *48*(17), e2021GL094679. https://doi.org/10.1029/2021GL094679

Thakur, P., Huang, Y., & Kaneko, Y. (2020). Effects of low-velocity fault damage zones on long-term earthquake behaviors on mature strike slip faults. *Journal of Geophysical Research: Solid Earth*, *125*(8), e2020JB019587. https://doi.org/10.1029/2020JB019587

Tong, P., Yao, J., Liu, Q., Li, T., Wang, K., Liu, S., et al. (2021). Crustal rotation and fluids: Factors for the 2019 Ridgecrest earthquake sequence? *Geophysical Research Letters*, *48*(3), e2020GL090853. https://doi.org/10.1029/2020GL090853

Weertman, J. J. (1980). Unstable slippage across a fault that separates elastic media of different elastic constants. *Journal of Geophysical Research*, *85*(B3), 1455–1461. https://doi.org/10.1029/jb085ib03p01455

Weertman, J. J. (2002). Subsonic type earthquake dislocation moving at approximately shear wave velocity on interface between half spaces of slightly different elastic constants. *Geophysical Research Letters*, *29*(10), 109-1–109-4. https://doi.org/10.1029/2001GL013916

Yang, H., Duan, Y., Song, J., Jiang, X., Tian, X., Yang, W., et al. (2020). Fine structure of the Chenghai fault zone, Yunnan, China constrained from teleseismic travel time and ambient noise tomography. *Journal of Geophysical Research: Solid Earth*, *125*(7) e2020JB019565. https://doi.org/10.1029/2020JB019565

Yeh, T., & Olsen, K. B. (2022). Data-constrained fault zone structure improves 0–3 Hz deterministic ground motion predictions for the 2019 M7.1 Ridgecrest earthquake. *Poster Presentation at 2022 SCEC Annual Meeting*. Retrieved from https://www.scec.org/meetings/2022/am/poster/226

Zhao, P., Peng, Z., Shi, Z., Lewis, M., & Ben-Zion, Y. (2010). Variations of the velocity contrast and rupture properties of M6 earthquakes along the Parkfield section of the San Andreas fault. *Geophysical Journal International*, *180*(2), 765–780. https://doi.org/10.1111/j.1365-246X.2009.04436.x

References From the Supporting Information

Crotwell, H. P., Owens, T. J., & Ritsema, J. (1999). The TauP Toolkit: Flexible seismic travel 90 time and ray-path utilities. *Seismological Research Letters*, *70*, 154–160. https://doi.org/10.1785/gssrl.70.2.154